

Loss-tolerant and supersensitive angular rotation estimation based on quantum-enhanced interferometers

Wenxiu Yao^{1,*}, Xiaoli Zhang^{1,*}, Long Tian^{1,2,†}, Xuan Liu¹, Shaoping Shi¹, and Yaohui Zheng^{1,2,‡}

¹*State Key Laboratory of Quantum Optics and Quantum Optics Devices, Institute of Opto-Electronics, Shanxi University, Taiyuan 030006, People's Republic of China*

²*Collaborative Innovation Center of Extreme Optics, Shanxi University, Taiyuan 030006, People's Republic of China*



(Received 16 May 2024; revised 27 June 2024; accepted 11 September 2024; published 23 September 2024)

Quantum resources have been proven to drive the measurement sensitivity to beyond standard quantum limit in quantum metrology. However, quantum advantage degrades with optical losses. Aiming at angular rotation estimation, we theoretically investigate three loss-tolerant (external loss) quantum-enhanced interferometers—the degenerate SU(1,1) interferometer (DSI), nondegenerate hybrid interferometer (NHI), and degenerate hybrid interferometer (DHI)—to achieve supersensitive angular rotation estimation, without strict requirement of external losses. Analysis results show that these interferometers are perfectly applicable to angular rotation estimation. Moreover, the sensitivity, which is the same as in the case of no external losses, can always be retrieved by taking full advantage of the second optical parametric amplifier as a phase-sensitive amplification. The sensitivity bound that originates from laser power restriction in the DSI scheme can be overcome by the employment of the NHI or DHI scheme. These results are critical in real time variation of the angle measurement and tracking an object in circular motion.

DOI: [10.1103/PhysRevA.110.032429](https://doi.org/10.1103/PhysRevA.110.032429)

I. INTRODUCTION

An interferometer, as one of the most sensitive measurement devices in the world, is the most basic tool in many scientific missions, from searching for dark matter [1] to gravitational wave detection [2–6]. Due to power requirements and the needs of advanced technologies, the measurement sensitivity of the interferometer continues to be driven to higher levels in the past years [7,8], extending the scope and depth of understanding of nature and the universe [9]. However, the behavior of measurement systems at small scales is governed by the laws of quantum mechanics; quantum properties of light place limits on the accuracy to which measurements can be performed, known as the standard quantum limit (SQL) [10]. It was Caves who in 1981 proposed to overcome the SQL and implement the supersensitive measurement by utilizing squeezed states with the fluctuation in one quadrature component below the SQL, without violating the Heisenberg uncertainty relation [11]. Subsequently, exploiting diverse quantum resources [12,13], quantum-enhanced interferometers with novel architecture were proposed and demonstrated to meet the requirement for a variety of application scenarios [14–22], expecting to reach the Heisenberg limit [23]. Unfortunately, the quantum state is very sensitive to losses; losses added during the detection process will inevitably limit metrological enhancement [24]. Relying on the second optical parametric amplifier (OPA) that serves as a phase-sensitive

optics amplification, a weak detection signal is magnified to become a loss-tolerant state, thereby relaxing detection requirements [25]. Similarly, the loss-tolerant detection scheme that relies on the reversal of quantum interactions has been also demonstrated in other physical systems [26–30]. However, the loss-tolerant proposal is confined to relatively few physical quantities, for example phase and displacement.

Angular rotation estimation, except for phase and displacement estimation, has been another topic of interest with a lot of potential applications, including quantum gyroscopes [31], accelerometers [32], and so on. Usually, angular rotation estimation is implemented by the employment of a light carrying orbital angular momentum (OAM) [33–38]. The OAM that a photon can have is quantized to integer multiples ℓ of \hbar , and is theoretically unbounded, so the light possessing OAM has emerged as a valuable experimental tool in imaging [39–41], optical communication [42–48], quantum information [49], quantum technologies [50,51], optical tweezers [52], and quantum detection [53–58]. In angular rotation estimation, utilizing photon OAM can amplify a mechanical rotation of ℓ into $\ell\theta$; thus, the sensitivity is enhanced by a factor of ℓ [59]. In 1998, Courtial *et al.* implemented the angular rotation estimation by the employment of OAM light and a Mach-Zehnder interferometer (MZI) [60]. Fickler *et al.* demonstrated that the entanglement photons with nonzero OAM can improve the sensitivity of angular-rotation measurement [61]. For another candidate of angular rotation estimation, the nondegenerate SU(1,1) interferometer, Liu *et al.* proposed the scheme that improves the sensitivity beyond SQL utilizing a quantum resource [62,63]. Following the work above, they investigated the dependence of the sensitivities of two different hybrid interferometers on interferometer parameters, showing a

*These authors contributed equally to this work.

†Contact author: tianlong@sxu.edu.cn

‡Contact author: yhzheng@sxu.edu.cn

negative influence of losses on the sensitivity [64]. Therefore, it is extremely urgent to propose some innovative schemes of angular rotation estimation with loss tolerance and supersensitivity.

In this paper, we investigate loss-tolerant (external loss) and supersensitive angular rotation estimation based on quantum-enhanced interferometers. Four different interferometers, including the traditional MZI, degenerate SU(1,1) interferometer (DSI), nondegenerate hybrid interferometer (NHI), and degenerate hybrid interferometer (DHI), are discussed. The sensitivity of the MZI is defined as SQL which is restricted by the vacuum fluctuations of the beam. Supposing that the quantum resource has a squeezing factor of 1.15, the sensitivity of the DHI can overcome SQL by 5 dB, which is higher than that of the NHI, and the DHI has a broader supersensitive range compared to the DSI scheme. The DHI and NHI can enhance sensitivity by increasing the power of coherent light injected into the bright port of interferometers, which is not restricted by nonlinear interaction in the DSI. However, the inevitable external losses of the interferometer will make the sensitivity dramatically worse. By taking full advantage of the second OPA as a phase-sensitive amplification, the sensitivity that is the same as in the case of no external losses can always be retrieved. These results provide valuable avenues for enhancing sensitivity and loss tolerance (external losses) of angular rotation estimation, which is of utmost importance in real time variation of the angle measurement and tracking an object in circular motion.

The paper is organized as follows. In Sec. II, we introduce four different interferometers for angular rotation estimation, and investigate their sensitivities. In Sec. III, we discuss the resolutions and sensitivities of these interferometers in the lossless scenario. The influences of interferometer system parameters, including OAM quanta momentum and phase-sensing light intensity on resolution and sensitivity, are analyzed. In Sec. IV, we study the influence of losses on resolution and sensitivity. Section V presents our conclusions.

II. MODELS OF ANGULAR ROTATION ESTIMATION

A. Scheme of the Mach-Zehnder interferometer

We first give a brief description of the MZI as shown in Fig. 1. A coherent beam \hat{a}_1 with amplitude $|\alpha_{\text{MZI}}| = \sqrt{N_{\hat{a}_1}}$ and a vacuum beam \hat{b}_1 pass through the first beam splitter (BS) with transmissivity T_1 . Then the beams after BS1 undergo the spiral phase plate (SPP) SPP1 and SPP2, respectively. The SPPs with a helical surface are used to introduce the OAM degree of freedom [65]. The optical thickness of the SPPs increases with azimuthal position. When the light fields pass through the SPPs, the linear momentum of the light acquires an azimuthal component that, when expressed with respect to a radius vector, gives an OAM of $\ell\hbar$ per photon [66]. The Dove prism (DP) is an optical element that rotates a beam carrying orbital angular momentum and also changes the sign of the beam's OAM mode index from ℓ to $-\ell$ [67]. In other words, the employment of DP1 and DP2 imposes phase shift of $2\ell\theta_{1,2}$ to the fields, denoted by $e^{-2i\ell\theta_{1,2}}$, where $\theta_{1,2}$ is the rotation angle of the DP1 or DP2 and is the parameter to be estimated in this paper. Then the beams undergo their OAM

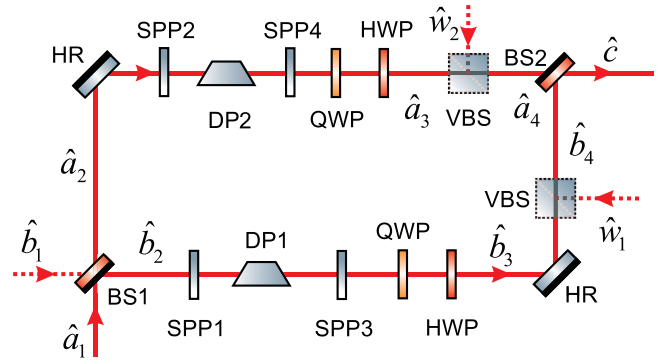


FIG. 1. Scheme for the angular rotation estimation by the employment of a Mach-Zehnder interferometer. BS, beam splitter; HR, high reflection mirror; SPP, spiral phase plate; DP, Dove prism; VBS, virtual beam splitter; HWP, half-wave plane; QWP, quarter-wave plane.

encoding with SPP3 or SPP4 of the same quanta number ℓ [59]. Finally, two beams are combined on BS2 with transmissivity T_2 , and one of the output ports can be selected to implement balanced homodyne detection (BHD). Note that the DP will introduce polarization change [68,69], and the polarization is dependent on the rotation angle of the DP. When a linearly polarized light (supposing that it is in S polarization) passes through two Dove prisms with equal and opposite rotations, the magnitude and direction of their vertical polarization components are the same. However, the horizontal polarization component has the same magnitude but opposite direction. Therefore, before the two beams are recombined, we can add a quarter-wave plate and half-wave plate and a removable polarization beam splitter (PBS) to ensure that the polarizations of both beams are the same. The operation process is as follows: at an unknown DP rotation angle, we place a removable PBS after two wave plates and then rotate two wave plates until the light power of P polarization is the least, then remove the PBS. At the moment, we can confirm that the beams are in S polarization, which ensures that the two beams from the two branches interfere at the BS2.

The input-output relations of BS1 are

$$\hat{a}_2 = \sqrt{T_1}\hat{a}_1 - \sqrt{R_1}\hat{b}_1, \quad (1)$$

$$\hat{b}_2 = \sqrt{T_1}\hat{b}_1 + \sqrt{R_1}\hat{a}_1, \quad (2)$$

where $T_1 + R_1 = 1$ is satisfied, T_1 and R_1 are the transmissivity and reflectivity of BS1, respectively; \hat{a}_1 and \hat{b}_1 are the annihilation operators of the coherent light and the vacuum state, respectively. The minus symbol in Eq. (1) is created by the phase difference caused by the half-wave loss. After BS1, the phase-sensing light intensity, i.e., the intensity of the phase-sensing field inside the interferometer, is [16]

$$I_{\text{PS}}^{\text{MZI}} = \langle \hat{b}_2^\dagger \hat{b}_2 \rangle + \langle \hat{a}_2^\dagger \hat{a}_2 \rangle = |\alpha_{\text{MZI}}|^2 = N_{\hat{a}_1}, \quad (3)$$

where $N_{\hat{a}_1} = |\alpha_{\text{MZI}}|^2 \gg 1$ is the photon number of the coherent light \hat{a}_1 .

Then, the beam's OAM degree of freedom is added by SPPs. Note that the SPPs are placed after the BS1, rather than before it, because the quanta number of OAM turns from ℓ

to $-\ell$ upon reflection. The optical fields passing through the SPPs and DPs are described as

$$\hat{a}_3 = \sqrt{T_1}e^{-2i\ell\theta_2}\hat{a}_1 - \sqrt{R_1}e^{-2i\ell\theta_2}\hat{b}_1, \quad (4)$$

$$\hat{b}_3 = \sqrt{T_1}e^{-2i\ell\theta_1}\hat{b}_1 + \sqrt{R_1}e^{-2i\ell\theta_1}\hat{a}_1. \quad (5)$$

After experiencing the internal losses $R_{\text{in}} = 1 - T_{\text{in}}$, the fields \hat{a}_3 and \hat{b}_3 become

$$\hat{a}_4 = \sqrt{T_1 T_{\text{in}}}e^{-2i\ell\theta_2}\hat{a}_1 - \sqrt{R_1 T_{\text{in}}}e^{-2i\ell\theta_2}\hat{b}_1 + \sqrt{R_{\text{in}}}\hat{w}_2, \quad (6)$$

$$\hat{b}_4 = \sqrt{T_1 T_{\text{in}}}e^{-2i\ell\theta_1}\hat{b}_1 + \sqrt{R_1 T_{\text{in}}}e^{-2i\ell\theta_1}\hat{a}_1 + \sqrt{R_{\text{in}}}\hat{w}_1, \quad (7)$$

where T_{in} and R_{in} are the transmissivity and reflectivity of the virtual beam splitter (VBS) which is used to simulate the internal losses on the interferometer's two branches. And $\hat{w}_{1,2}$ are the corresponding introduced vacuum noises.

For simplicity, we consider a balanced case, i.e., $T_1 = T_2 = 0.5$, and the angles of two DPs satisfy $\theta_1 = -\theta_2 = \theta$; the input-output relation of the MZI is described by [70]

$$\hat{c} = i\sin(2\ell\theta)\sqrt{T_{\text{in}}}\hat{a}_1 - \cos(2\ell\theta)\sqrt{T_{\text{in}}}\hat{b}_1 + \sqrt{R_{\text{in}}}\hat{w}_-, \quad (8)$$

where $\hat{w}_- = (\hat{w}_2 - \hat{w}_1)/\sqrt{2}$.

In this case, we use the BHD method to continue the measurements. The measurement operator is the quadrature amplitude operator \hat{X} at the output port \hat{c} which can be expressed as

$$\hat{X} = -\sin(2\ell\theta)\sqrt{T_{\text{in}}}\hat{Y}_{\hat{a}_1} - \cos(2\ell\theta)\sqrt{T_{\text{in}}}\hat{X}_{\hat{b}_1} + \sqrt{R_{\text{in}}}\hat{X}_{\hat{w}_-}. \quad (9)$$

In order to get the quantum fluctuations on quadrature amplitude, we calculate the expected value $\langle \hat{X} \rangle$ which can be expressed as

$$\langle \hat{X} \rangle = -\sin(2\ell\theta)\sqrt{T_{\text{in}}|\alpha_{\text{MZI}}|} = -\sin(2\ell\theta)\sqrt{T_{\text{in}}I_{\text{PS}}^{\text{MZI}}}. \quad (10)$$

The variance of the quadrature amplitude operator is given by

$$\langle \delta^2 \hat{X} \rangle = \langle \hat{X}^2 \rangle - \langle \hat{X} \rangle^2 = 1. \quad (11)$$

An important evaluation criterion is the visibility of parameter estimation. In terms of definition of visibility [15],

$$V = \frac{\langle \hat{X} \rangle_{\text{max}} - \langle \hat{X} \rangle_{\text{min}}}{|\langle \hat{X} \rangle_{\text{max}}| + |\langle \hat{X} \rangle_{\text{min}}|}, \quad (12)$$

where $\langle \hat{X} \rangle_{\text{max}}$ and $\langle \hat{X} \rangle_{\text{min}}$ mean the maximum and minimum values of $\langle \hat{X} \rangle$. We can find that the MZI has 100% visibility.

For the sensitivity of angular rotation estimation, it can be derived as

$$\delta\theta_{\text{MZI}} = \frac{\sqrt{\langle \delta^2 \hat{X} \rangle}}{|\partial \langle \hat{X} \rangle / \partial \theta|} = \frac{1}{2|\ell|\cos(2\ell\theta)\sqrt{T_{\text{in}}I_{\text{PS}}^{\text{MZI}}}}. \quad (13)$$

It is shown that the sensitivity depends on not only the phase-sensing light intensity $I_{\text{PS}}^{\text{MZI}}$ but also OAM quanta number ℓ . And it is relatively easy to prepare the state $|\ell| \geq 10$ under the current experimental condition, indicating that, while $I_{\text{PS}}^{\text{MZI}}$ remains unchanged, this approach has an enhanced effect of

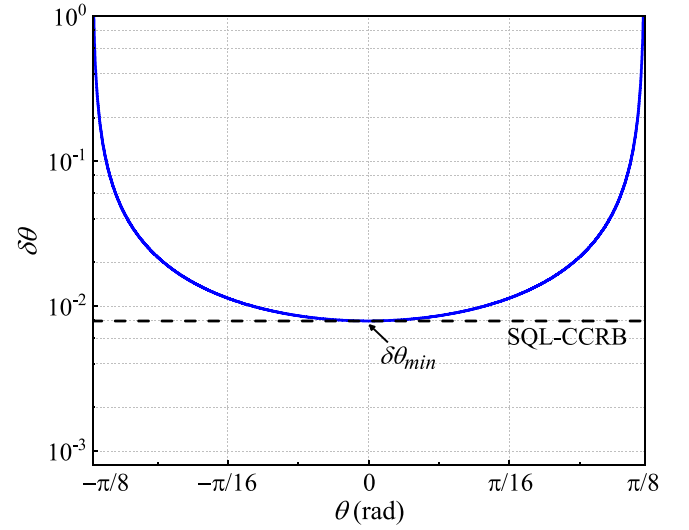


FIG. 2. Angular rotation sensitivity of the MZI (Fig. 1) as a function of the phase shift θ of the Dove prism, for the parameters $I_{\text{PS}}^{\text{MZI}} = 10^3$ and $\ell = 2$. The optimal angular rotation sensitivity $\delta\theta_{\text{min}}$ is obtained at $\theta = 0$. The supersensitive angular rotation range $\Delta = 0$.

about one to two orders of magnitude compared with non-OAM systems.

In the case of no internal losses ($T_{\text{in}} = 1$), we can see the optimal sensitivity of the MZI appears when the interferometer is operating at the dark fringe $2\ell\theta = 0$ from Fig. 2. Assuming a relatively weak angular rotation is introduced, the optimal sensitivity is given by

$$\delta\theta_{\text{SQL}} = \frac{1}{2|\ell|\sqrt{I_{\text{PS}}^{\text{MZI}}}}. \quad (14)$$

This restriction is known as SQL, due to the Poissonian photon statistics of the coherent quantum state. However, the SQL can be overcome by means of nonclassical-states injection which can reduce the noise inside the interferometer. We will discuss this in the following sections.

Except for $\delta\theta_{\text{min}}$, another important figure of merit is angular rotation range Δ where the sensitivity exceeds the SQL, i.e., the supersensitive range. According to Eqs. (13) and (14), the supersensitive range of the MZI is zero.

In addition, the lower bound of the achievable precision in the estimation of θ is provided by the classical Cramér-Rao theorem; the classical Cramér-Rao bound (CCRB) can be expressed as

$$\Delta\theta_{\text{CCRB}}^{\text{MZI}} = \frac{1}{\sqrt{F_\theta}}, \quad (15)$$

where F_θ is the Fisher information:

$$F_\theta = \frac{(\partial \langle \hat{X} \rangle / \partial \theta)^2 + 2(\partial \langle \delta^2 \hat{X} \rangle / \partial \theta)^2}{\langle \delta^2 \hat{X} \rangle}. \quad (16)$$

Notice that $\langle \delta^2 \hat{X} \rangle = 1$ for the MZI. Therefore, we obtain $\delta\theta_{\text{MZI}} = \Delta\theta_{\text{CCRB}}^{\text{MZI}} = 1/\sqrt{F_\theta}$. In other words, the sensitivity is equal to the CCRB for the MZI.

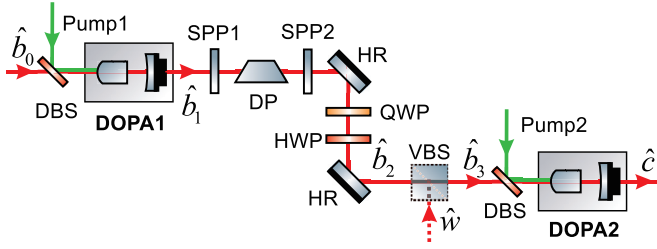


FIG. 3. Scheme for angular rotation estimation by the employment of a degenerate SU(1,1) interferometer. The green line indicates that the beam is a pump beam. A squeezed state is generated from a degenerate optical parameter amplifier (DOPA1), and its OAM degree of freedom is added by a SPP1. Subsequently, when the beam passes through a DP with angular rotation θ , it will have a phase shift of $2\ell\theta$. DBS, dichroic beam splitter.

B. Scheme of the degenerate SU(1,1) interferometer

Now, let us consider a DSI consisting of two degenerate optical parameter amplifiers (DOPAs) [71], as shown in Fig. 3. For convenience, we take the Heisenberg picture. The relationship between input and output of the DOPA is

$$\hat{b}_1 = \sqrt{G_1} \hat{b}_0 - \sqrt{G_1 - 1} e^{i\phi_1} \hat{b}_0^\dagger, \quad (17)$$

where $G_1 = \cosh^2 r_1$ is the amplitude gain of the DOPA1 with squeezing factor r_1 . We suppose here that a coherent seed beam \hat{b}_0 with an amplitude $|\alpha_{\text{DSI}}| \gg 1$ is injected into the DOPA1 and the relative phase between the seed beam and the pump beam $\phi_1 = 0$. For the above DSI, we can calculate $I_{\text{PS}}^{\text{DSI}}$ as

$$I_{\text{PS}}^{\text{DSI}} \approx (2\cosh^2 r_1 - 1) |\alpha_{\text{DSI}}|^2. \quad (18)$$

Subsequently, the beam through SPPs and DP is given by

$$\hat{b}_2 = \sqrt{G_1} e^{-2i\ell\theta} \hat{b}_0 - \sqrt{G_1 - 1} e^{-2i\ell\theta} \hat{b}_0^\dagger. \quad (19)$$

Then a VBS is used to simulate the internal loss:

$$\hat{b}_3 = \sqrt{T_{\text{in}} G_1} e^{-2i\ell\theta} \hat{b}_0 - \sqrt{T_{\text{in}} (G_1 - 1)} e^{-2i\ell\theta} \hat{b}_0^\dagger + \sqrt{R_{\text{in}}} \hat{w}. \quad (20)$$

The DOPA2 with opposite phase $\phi_2 = \pi$ is placed in the downstream path. The relationship between input and output beams of the DSI has the following form:

$$\begin{aligned} \hat{c} = & \sqrt{T_{\text{in}}} [\sqrt{G_1 G_2} e^{-2i\ell\theta} - \sqrt{(G_1 - 1)(G_2 - 1)} e^{2i\ell\theta}] \hat{b}_0 \\ & + \sqrt{T_{\text{in}}} [\sqrt{G_1 (G_2 - 1)} e^{2i\ell\theta} - \sqrt{(G_1 - 1) G_2} e^{-2i\ell\theta}] \hat{b}_0^\dagger \\ & + \sqrt{R_{\text{in}} G_2} \hat{w} + \sqrt{R_{\text{in}} (G_2 - 1)} \hat{w}^\dagger, \end{aligned} \quad (21)$$

where $G_2 = \cosh^2 r_2$ is the amplitude gain of the DOPA2 with the squeezing factor r_2 . The amplitude quadrature of the output beam is

$$\begin{aligned} \hat{X} = & e^{r_1 + r_2} \sin(2\ell\theta) \sqrt{T_{\text{in}}} \hat{Y}_{\hat{b}_0} + e^{r_2 - r_1} \cos(2\ell\theta) \sqrt{T_{\text{in}}} \hat{X}_{\hat{b}_0} \\ & + e^{r_2} \sqrt{R_{\text{in}}} \hat{X}_{\hat{w}}. \end{aligned} \quad (22)$$

The output signal is given by the expected value of \hat{X} :

$$\langle \hat{X} \rangle = e^{r_1 + r_2} \sin(2\ell\theta) \sqrt{T_{\text{in}}} |\alpha_{\text{DSI}}|. \quad (23)$$

According to Eq. (12), we can calculate that the DSI visibility is 100%. Then, the variance of the quadrature amplitude operator is

$$\langle \delta^2 \hat{X} \rangle = e^{2r_2} \{ [e^{2r_1} \sin^2(2\ell\theta) + e^{-2r_1} \cos^2(2\ell\theta)] T_{\text{in}} + R_{\text{in}} \}. \quad (24)$$

Based on Eqs. (23) and (24), the sensitivity of angular rotation estimation for the DSI is given by

$$\delta\theta_{\text{DSI}} = \frac{\sqrt{[\tan^2(2\ell\theta) + e^{-4r_1}] T_{\text{in}} + R_{\text{in}} / e^{2r_1} \cos^2(2\ell\theta)}}{2|\ell| \sqrt{T_{\text{in}} I_{\text{PS}}^{\text{DSI}} / (2\cosh^2 r_1 - 1)}}. \quad (25)$$

Then, supposing that the internal loss is zero, the supersensitivity range is

$$\Delta_{\text{DSI}} = \frac{1}{|\ell|} \arctan \sqrt{\frac{1}{2\cosh^2 r_1 - 1} - e^{-4r_1}}. \quad (26)$$

It is clear that the gain of the DOPA2 has no effect on the sensitivity of the DSI in a lossless scenario. But the increase of $I_{\text{PS}}^{\text{DSI}}$ or $|\ell|$ can provide an enhanced sensitivity. To increase phase-sensing light intensity $I_{\text{PS}}^{\text{DSI}}$, a seed light is introduced into the DOPA1 to stimulate the generation of bright squeezed states. While the DOPA process can be noiseless in theory, it inevitably introduces noise as the seed beam power is increased due to the coupling between the pump and seed field [72]. This drawback has to date limited the phase-sensing light power to few microwatts in the DSI, thereby setting an intrinsic limit to sensitivity [27].

We now briefly review how to calculate the quantum Fisher information (QFI) and the quantum Cramér-Rao bound (QCRB). According to Refs. [17,73,74], the QCRB can be obtained by transforming the expected values and covariance matrix from the quadrature operator basis to the annihilation operator basis. We introduce the quadrature column operators

$$\vec{X}_{\text{DSII}} = (0 \quad |\alpha_{\text{DSI}}| \quad 0 \quad 0)^T, \quad (27)$$

and the symmetric covariance matrix can be expressed as

$$\Gamma_1 = \begin{pmatrix} 1 & 0 & 0 & 0 \\ 0 & 1 & 0 & 0 \\ 0 & 0 & 1 & 0 \\ 0 & 0 & 0 & 1 \end{pmatrix}. \quad (28)$$

The transformations through the DP-SPP and two OPAs can be given by

$$S_\theta = \begin{pmatrix} \cos(2\ell\theta) & -\sin(2\ell\theta) & 0 & 0 \\ \sin(2\ell\theta) & \cos(2\ell\theta) & 0 & 0 \\ 0 & 0 & \cos(2\ell\theta) & \sin(2\ell\theta) \\ 0 & 0 & -\sin(2\ell\theta) & \cos(2\ell\theta) \end{pmatrix}, \quad (29)$$

$$S_{\text{DOPA1}} = \begin{pmatrix} e^{-r_1} & 0 & 0 & 0 \\ 0 & e^{r_1} & 0 & 0 \\ 0 & 0 & e^{-r_1} & 0 \\ 0 & 0 & 0 & e^{r_1} \end{pmatrix}, \quad (30)$$

$$S_{\text{DOPA2}} = \begin{pmatrix} e^{r_2} & 0 & 0 & 0 \\ 0 & e^{-r_2} & 0 & 0 \\ 0 & 0 & e^{r_2} & 0 \\ 0 & 0 & 0 & e^{-r_2} \end{pmatrix}, \quad (31)$$

where we have considered the balanced situation that $\phi_1 = 0$, $\phi_2 = \pi$, and $\theta_1 = -\theta_2 = \theta$. Therefore, the transformation matrix for the DSI can be obtained as $S_{\text{DSI}} = S_{\text{DOPA2}} S_{\theta} S_{\text{DOPA1}}$.

The column vector of the expected value of the quadrature \bar{X}_{DSI2} and the symmetric covariance matrix of the quadrature Γ_{DSI2} for the output states of the DSI are

$$\bar{X}_{\text{DSI2}} = S_{\text{DSI}} \bar{X}_{\text{DSI1}}, \quad (32)$$

$$\Gamma_{\text{DSI2}} = S_{\text{DSI}} \Gamma_1 S_{\text{DSI}}^T. \quad (33)$$

In the following we transform the expected values and covariance matrix from the quadrature operator basis to the annihilation operator basis. For the creation and annihilation operator vector of the output state \hat{d} , the expected value can be obtained:

$$\bar{d} = H \bar{X}_{\text{DSI2}} = |\alpha_{\text{DSI}}| \begin{pmatrix} -e^{r_1+r_2} \sin(2\ell\theta) \\ e^{r_1-r_2} \cos(2\ell\theta) \\ 0 \\ 0 \end{pmatrix}, \quad (34)$$

where the transformation matrix H is used to transform the expected value and covariance matrix from the quadrature operator basis to the annihilation operator basis, and is expressed as

$$H = \frac{1}{2} \begin{pmatrix} 1 & i & 0 & 0 \\ 1 & -i & 0 & 0 \\ 0 & 0 & 1 & i \\ 0 & 0 & 1 & -i \end{pmatrix}. \quad (35)$$

Similarly, we can obtain the covariance matrix for the DSI:

$$\Sigma = H \Gamma_{\text{DSI2}} H^T. \quad (36)$$

According to Ref. [73], the QFI describes the phase-sensing potential of the quantum state in the interferometer, which is given by

$$F_Q^{\text{DSI}} = \frac{1}{2} \text{Tr} \left\{ \frac{\partial \Sigma}{\partial \theta} \left[\Sigma \left(\frac{\partial \Sigma}{\partial \theta} \right)^{-1} \Sigma^T + \frac{1}{4} J \left(\frac{\partial \Sigma}{\partial \theta} \right)^{-1} J^T \right]^{-1} \right\} + \left(\frac{\partial \bar{d}}{\partial \theta} \right)^T \Sigma^{-1} \frac{\partial \bar{d}}{\partial \theta} \\ = 16\ell^2 \sinh(2r_1)^2 + 4\ell^2 e^{4r_1} |\alpha_{\text{DSI}}|^2 \\ = 16\ell^2 \sinh(2r_1)^2 + 4\ell^2 e^{4r_1} I_{\text{PS}}^{\text{DSI}} / (2\cosh^2 r_1 - 1), \quad (37)$$

where J can be expressed as

$$J = \begin{pmatrix} 0 & 1 & 0 & 0 \\ -1 & 0 & 0 & 0 \\ 0 & 0 & 0 & 1 \\ 0 & 0 & -1 & 0 \end{pmatrix}. \quad (38)$$

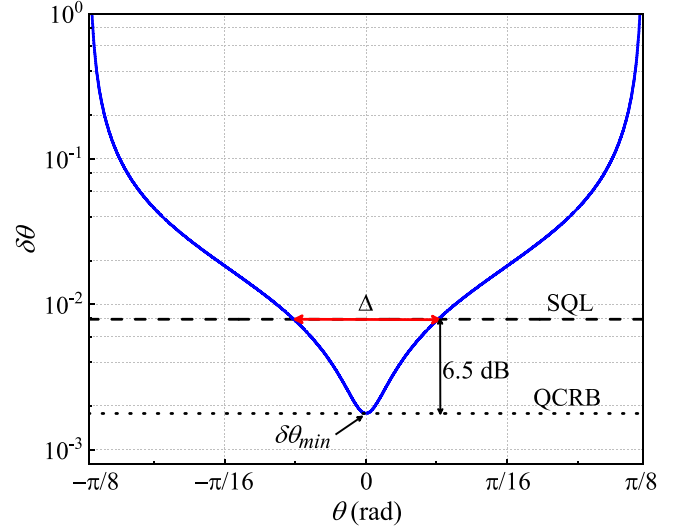


FIG. 4. Angular rotation sensitivity of a seeded degenerate $SU(1,1)$ interferometer (Fig. 3) as a function of angular rotation, for the parameters $r_1 = r_2 = 1.15$, $I_{\text{PS}}^{\text{DSI}} = 10^3$, and $\ell = 2$. The optimal angular rotation sensitivity $\delta\theta_{\min}$ is obtained at $\theta = 0$. The supersensitive angular rotation range Δ is shown (red arrow).

Then the corresponding QCRB is given by

$$\Delta\theta_{\text{QCRB}}^{\text{DSI}} = 1/\sqrt{F_Q^{\text{DSI}}}. \quad (39)$$

Figure 4 shows the sensitivity $\delta\theta_{\text{DSI}}$ ($T_{\text{in}} = 1$) and the $\Delta\theta_{\text{QCRB}}^{\text{DSI}}$, as a function of the angular rotation θ with the parameters $r_1 = r_2 = 1.15$ and $\ell = 2$. Since the sensitivity of an interferometer is related to the photon number inside the interferometer, for a fair comparison between the DSI and MZI, we set $I_{\text{PS}}^{\text{DSI}} = I_{\text{PS}}^{\text{MZI}} = 10^3$, which can be achieved by adjusting α_{DSI} and α_{MZI} independently. We obtain that the sensitivity of the DSI is 6.5 dB higher than that of the MZI and the supersensitive range is $\Delta_{\text{DSI}} \approx \pi/16$ in this case. Obviously, comparing the result with SQL, it is easy to find that with the help of the DOPA the optimal angular rotation sensitivity is enhanced by a factor of $\sqrt{2\cosh^2 r_1 - 1}e^{-2r_1}$.

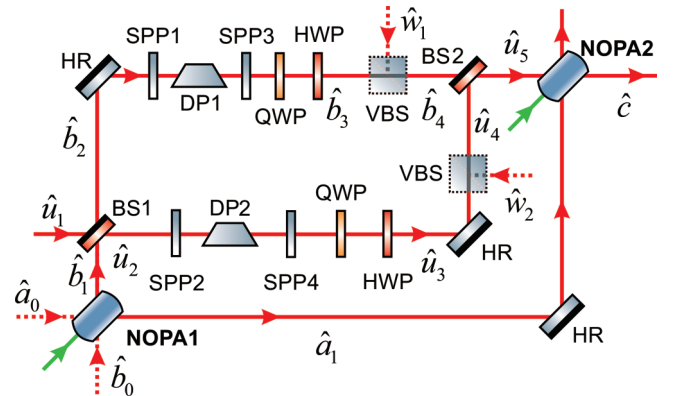


FIG. 5. Scheme for the angular rotation estimation by the employment of a nondegenerate hybrid interferometer. NOPA, nondegenerate optical parameter amplifier.

C. Scheme of the nondegenerate hybrid interferometer

In this section, we consider another construction in which a MZI and two nondegenerate optical parameter amplifiers (NOPAs) construct an NHI, as shown in Fig. 5.

A NOPA is used to generate twin beams \hat{a}_1 and \hat{b}_1 . According to quantum optics, the input and output of the NOPA have the relations

$$\hat{a}_1 = i\sqrt{G_1}\hat{a}_0 + i\sqrt{G_1 - 1}\hat{b}_0^\dagger, \quad (40)$$

$$\hat{b}_1 = i\sqrt{G_1 - 1}\hat{a}_0^\dagger + i\sqrt{G_1}\hat{b}_0. \quad (41)$$

Then the signal beam \hat{b}_1 from the NOPA1 is fed into the MZI dark input port, and is recombined with a coherent light \hat{u}_1 with amplitude $|\alpha_{\text{NHI}}|$ on BS1; the operators can be expressed as

$$\hat{b}_2 = \sqrt{R_1}\hat{u}_1 + \sqrt{T_1}\hat{b}_1, \quad (42)$$

$$\hat{u}_2 = \sqrt{T_1}\hat{u}_1 - \sqrt{R_1}\hat{b}_1. \quad (43)$$

And the phase sensing field intensity is

$$I_{\text{PS}}^{\text{NHI}} = |\alpha_{\text{NHI}}|^2 = N_{\hat{u}_1}. \quad (44)$$

After the beams traversing the SPPs and DPs have the following forms:

$$\hat{b}_3 = e^{-2i\ell\theta_1}\hat{b}_2, \quad (45)$$

$$\hat{u}_3 = e^{-2i\ell\theta_2}\hat{u}_2. \quad (46)$$

The beams experience the internal loss:

$$\hat{b}_4 = \sqrt{T_{\text{in}}}\hat{b}_3 + \sqrt{R_{\text{in}}}\hat{w}_1, \quad (47)$$

$$\hat{u}_4 = \sqrt{T_{\text{in}}}\hat{u}_3 + \sqrt{R_{\text{in}}}\hat{w}_2. \quad (48)$$

Then they are recombined on the BS2:

$$\hat{u}_5 = \sqrt{T_2}\hat{b}_4 - \sqrt{R_2}\hat{u}_4. \quad (49)$$

The light \hat{u}_5 emerging from the MZI dark output port is then recombined with the idler beam \hat{a}_1 in the NOPA2. The output field of the NHI is

$$\begin{aligned} \hat{c} = & \sqrt{T_{\text{in}}G_2}(\sqrt{R_1T_2}e^{-2i\ell\theta_1} - \sqrt{T_1R_2}e^{-2i\ell\theta_2})\hat{c}_1 + i(\sqrt{T_1T_2}e^{-2i\ell\theta_1} + \sqrt{R_1R_2}e^{-2i\ell\theta_2})\sqrt{T_{\text{in}}G_2(G_1 - 1)}\hat{a}_0^\dagger \\ & - i\sqrt{G_1(G_2 - 1)}\hat{a}_0^\dagger - i\sqrt{(G_1 - 1)(G_2 - 1)}\hat{b}_0 + i\sqrt{T_{\text{in}}G_1G_2}(\sqrt{T_1T_2}e^{-2i\ell\theta_1} + \sqrt{R_1R_2}e^{-2i\ell\theta_2})\hat{b}_0 \\ & + \sqrt{R_{\text{in}}T_2G_2}\hat{w}_1 - \sqrt{R_{\text{in}}R_2G_2}\hat{w}_2. \end{aligned} \quad (50)$$

Supposing that $\theta_1 = -\theta_2 = \theta$ and $T_1 = T_2 = 0.5$, the amplitude quadrature operator of the output field can be calculated as

$$\begin{aligned} \hat{X} = & \sqrt{T_{\text{in}}G_2}\sin(2\ell\theta)\hat{Y}_{\hat{u}_1} - \sqrt{R_{\text{in}}G_2}\hat{X}_{\hat{w}_-} + [\sqrt{T_{\text{in}}G_2(G_1 - 1)}\cos(2\ell\theta) - \sqrt{G_1(G_2 - 1)}]\hat{Y}_{\hat{a}_0} \\ & + [\sqrt{(G_1 - 1)(G_2 - 1)} - \sqrt{T_{\text{in}}G_1G_2}\cos(2\ell\theta)]\hat{Y}_{\hat{b}_0}. \end{aligned} \quad (51)$$

The output signal, i.e., the expected value of the amplitude quadrature of the NHI, is

$$\langle \hat{X} \rangle = \sqrt{T_{\text{in}}G_2}\sin(2\ell\theta)|\alpha_{\text{NHI}}|. \quad (52)$$

We can calculate that the visibility of the NHI is 100%.

Next, we calculate the associated uncertainty $\langle \delta^2 \hat{X} \rangle$ of the output beam, the sensitivity of angular rotation estimation, and the supersensitive range in the lossless scenario, i.e., $T_{\text{in}} = 1$ for the NHI:

$$\begin{aligned} \langle \delta^2 \hat{X} \rangle = & T_{\text{in}}G_2\sin^2(2\ell\theta) + R_{\text{in}}G_2 + [\sqrt{T_{\text{in}}G_2(G_1 - 1)}\cos(2\ell\theta) - \sqrt{G_1(G_2 - 1)}]^2 + [\sqrt{(G_1 - 1)(G_2 - 1)} \\ & - \sqrt{T_{\text{in}}G_1G_2}\cos(2\ell\theta)]^2, \end{aligned} \quad (53)$$

$$\begin{aligned} \delta\theta_{\text{NHI}} = & \{R_{\text{in}}G_2 + T_{\text{in}}G_2\sin^2(2\ell\theta) + [T_{\text{in}}G_2\cos^2(2\ell\theta) + G_2 - 1](2G_1 - 1) \\ & - 4\sqrt{T_{\text{in}}G_1G_2(G_1 - 1)(G_2 - 1)}\cos(2\ell\theta)\}^{\frac{1}{2}} / [2|\ell|\sqrt{T_{\text{in}}G_2}\cos(2\ell\theta)\sqrt{I_{\text{PS}}^{\text{NHI}}}], \end{aligned} \quad (54)$$

$$\Delta = \frac{1}{|\ell|} \arctan[2(1 - G_1) + 4\sqrt{G_1(G_1 - 1)(G_2 - 1)/G_2} - (2G_1 - 1)(G_2 - 1)/G_2]^{\frac{1}{2}}. \quad (55)$$

For the NHI, the transformation through the BS, the NOPA, and the phase shift can be given by

$$S_{\text{BS}} = \begin{pmatrix} \sqrt{\frac{1}{2}} & 0 & -\sqrt{\frac{1}{2}} & 0 \\ 0 & \sqrt{\frac{1}{2}} & 0 & -\sqrt{\frac{1}{2}} \\ \sqrt{\frac{1}{2}} & 0 & \sqrt{\frac{1}{2}} & 0 \\ 0 & \sqrt{\frac{1}{2}} & 0 & \sqrt{\frac{1}{2}} \end{pmatrix}, \quad (56)$$

$$S_\theta = \begin{pmatrix} \cos(2\ell\theta) & -\sin(2\ell\theta) & 0 & 0 \\ \sin(2\ell\theta) & \cos(2\ell\theta) & 0 & 0 \\ 0 & 0 & \cos(2\ell\theta) & \sin(2\ell\theta) \\ 0 & 0 & -\sin(2\ell\theta) & \cos(2\ell\theta) \end{pmatrix}, \quad (57)$$

$$S_{\text{NOPA1}} = \begin{pmatrix} 0 & -\cosh r_1 & 0 & \sinh r_1 \\ \cosh r_1 & 0 & \sinh r_1 & 0 \\ 0 & \sinh r_1 & 0 & -\cosh r_1 \\ \sinh r_1 & 0 & \cosh r_1 & 0 \end{pmatrix}, \quad (58)$$

$$S_{\text{NOPA2}} = \begin{pmatrix} \cosh r_2 & 0 & \sinh r_2 & 0 \\ 0 & \cosh r_2 & 0 & -\sinh r_2 \\ \sinh r_2 & 0 & \cosh r_2 & 0 \\ 0 & -\sinh r_2 & 0 & \cosh r_2 \end{pmatrix}. \quad (59)$$

The column vector of expected values of the quadratures for the output states is

$$\bar{X}_{\text{NHI2}} = S_{\text{NHI1}} \bar{X}_{\text{DSI1}} = S_{\text{NOPA2}} S_{\text{BS}} S_\theta S_{\text{BS}} \bar{X}_{\text{NHI1}} \quad (60)$$

where $\bar{X}_{\text{NHI1}} = (0 \mid \alpha_{\text{NHI}} \mid 0 \ 0)^T$. And the input-output relation of the symmetric covariance matrix of the quadratures is

$$\Gamma_{\text{NHI2}} = S_{\text{NHI2}} \Gamma_1 S_{\text{NHI2}}^T, \quad (61)$$

where $S_{\text{NHI2}} = S_{\text{NOPA2}} S_{\text{BS}} S_\theta S_{\text{BS}} S_{\text{NOPA1}}$.

Then the QFI of the NHI can be obtained as

$$\begin{aligned} F_Q^{\text{NHI}} &= 4\ell^2 [|\alpha_{\text{NHI}}|^2 \cosh(2r_1) + 4\cosh^2(2r_1) - 4] \\ &= 4\ell^2 [I_{\text{PS}}^{\text{NHI}} \cosh(2r_1) + 4\cosh^2(2r_1) - 4]. \end{aligned} \quad (62)$$

According to Eq. (39), we can obtain the corresponding QCRB of the NHI, as shown in Fig. 6.

Although the sensitivity of the NHI can beat SQL by 3.5 dB, it is worse than that of the DSI as shown in Fig. 6. However, the NHI has broader supersensitive range Δ , which is approximately $\pi/8$, due to the introduction of the MZI.

D. Scheme of the degenerate hybrid interferometer

In order to further improve the sensitivity of angular rotation without affecting the supersensitive range, we introduce a DHI scheme, as shown in Fig. 7. A squeezed vacuum from the DOPA1 is injected into the MZI dark port to reduce noise of the whole loop; the bright port is fed with coherent light with an amplitude $|\alpha_{\text{DHI}}|$. The SPPs and DP are placed in both arms. Finally, the MZI dark port output is amplified by the DOPA2 and then measured. Here, for the sake of completeness, we consider the measurement of the amplitude quadrature by means of a balanced homodyne detector. For the DHI, these are

$$\hat{b}_1 = \sqrt{G_1} \hat{b}_0 - \sqrt{G_1 - 1} e^{i\phi_1} \hat{b}_0^\dagger, \quad (63)$$

$$\hat{a}_2 = \sqrt{T_1} \hat{a}_1 - \sqrt{R_1} \hat{b}_1, \quad \hat{b}_2 = \sqrt{R_1} \hat{a}_1 + \sqrt{T_1} \hat{b}_1, \quad (64)$$

$$\hat{a}_3 = e^{-2i\ell\theta_2} \hat{a}_2, \quad \hat{b}_3 = e^{-2i\ell\theta_1} \hat{b}_2, \quad (65)$$

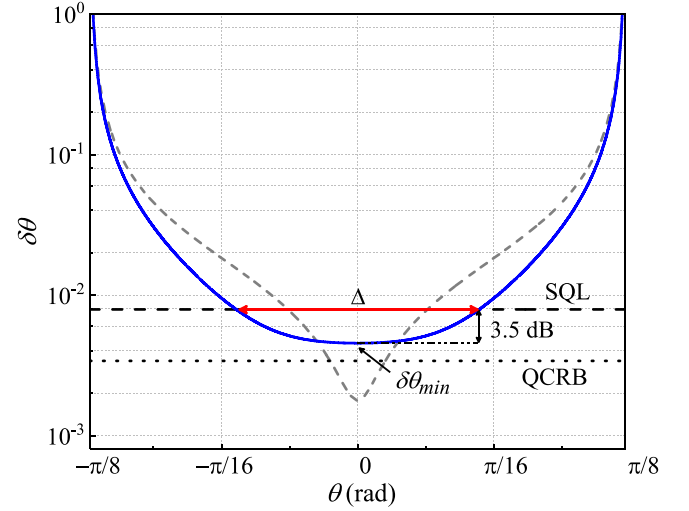


FIG. 6. Angular rotation sensitivity of a nondegenerate hybrid interferometer (Fig. 5) as a function of angular rotation θ , for the parameters $r_1 = r_2 = 1.15$, $I_{\text{PS}}^{\text{NHI}} = 10^3$, and $\ell = 2$. The optimal angular rotation sensitivity $\delta\theta_{\text{min}}$ is obtained at $\theta = 0$. The supersensitive angular rotation range Δ is shown (red arrow). For comparison, the angular rotation sensitivity of the DSI (gray dashed line) from Fig. 4 is plotted as well.

$$\hat{a}_4 = \sqrt{T_{\text{in}}} \hat{a}_3 + \sqrt{R_{\text{in}}} \hat{w}_2, \quad \hat{b}_4 = \sqrt{T_{\text{in}}} \hat{b}_3 + \sqrt{R_{\text{in}}} \hat{w}_1, \quad (66)$$

$$\hat{a}_5 = \sqrt{T_2} \hat{a}_4 - \sqrt{R_2} \hat{b}_4, \quad (67)$$

$$\hat{c} = \sqrt{G_2} \hat{a}_5 - \sqrt{G_2 - 1} e^{i\phi_2} \hat{a}_5^\dagger. \quad (68)$$

And $I_{\text{PS}}^{\text{DHI}}$ is

$$I_{\text{PS}}^{\text{DHI}} = N_{\hat{a}_1}. \quad (69)$$

Here we suppose $T_1 = T_2 = 0.5$, $\phi_1 = 0$, $\phi_2 = \pi$, $\theta_1 = -\theta_2 = \theta$, and the output field \hat{c} is simplified to

$$\begin{aligned} \hat{c} &= i\sin(2\ell\theta) \sqrt{T_{\text{in}}} (\sqrt{G_2} \hat{a}_1 - \sqrt{G_2 - 1} \hat{a}_1^\dagger) \\ &+ \sqrt{T_{\text{in}}} [\sqrt{(G_1 - 1)(G_2 - 1)} - \sqrt{G_1 G_2}] \cos(2\ell\theta) \hat{b}_0 \\ &+ \sqrt{T_{\text{in}}} [\sqrt{(G_1 - 1)G_2} - \sqrt{G_1(G_2 - 1)}] \cos(2\ell\theta) \hat{b}_0^\dagger \\ &+ \sqrt{R_{\text{in}}} (\sqrt{G_2} \hat{w}_- + \sqrt{G_2 - 1} \hat{w}_-^\dagger). \end{aligned} \quad (70)$$

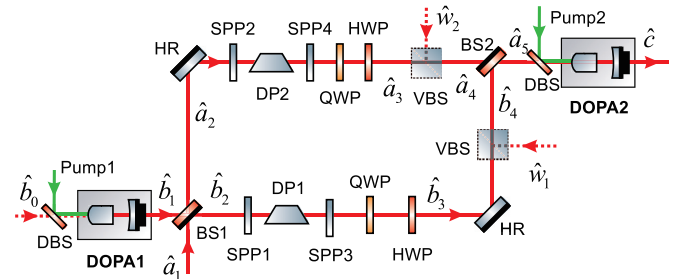


FIG. 7. Scheme for the angular rotation estimation by the employment of a degenerate hybrid interferometer.

The amplitude quadrature is given by

$$\hat{X} = -\sin(2\ell\theta)e^{r_2}\sqrt{T_{\text{in}}}\hat{X}_{a_1} + \sqrt{R_{\text{in}}}e^{r_2}\hat{X}_{a_2} + e^{r_2-r_1}\cos(2\ell\theta)\sqrt{T_{\text{in}}}\hat{X}_{b_0}. \quad (71)$$

The output signal is

$$\langle \hat{X} \rangle = -\sin(2\ell\theta)e^{r_2}\sqrt{T_{\text{in}}|\alpha_{\text{DHI}}|. \quad (72)$$

From Eq. (12), we obtain that the visibility of the interferometer can be obtained as 100%. The noise variance is

$$\langle \delta^2 \hat{X} \rangle = [\sin^2(2\ell\theta) + \cos^2(2\ell\theta)e^{-2r_1}]T_{\text{in}} + R_{\text{in}}e^{2r_2}. \quad (73)$$

The sensitivity for the angular rotation estimate is

$$\delta\theta_{\text{DHI}} = \frac{\sqrt{[\sin^2(2\ell\theta) + \cos^2(2\ell\theta)e^{-2r_1}]T_{\text{in}} + R_{\text{in}}}}{2|\ell|\cos(2\ell\theta)\sqrt{T_{\text{in}}|\alpha_{\text{DHI}}|}. \quad (74)$$

And the supersensitive range (in the lossless situation $T_{\text{in}} = 1$) is

$$\Delta_{\text{DHI}} = \frac{1}{|\ell|} \arctan \sqrt{1 - e^{-2r_1}}. \quad (75)$$

In addition, due to the DOPA1 a squeezed vacuum state is generated, so the transformation through the DOPA1 and the BS for the DHI can be given by

$$S_{\text{DOPA1}} = \begin{pmatrix} 1 & 0 & 0 & 0 \\ 0 & 1 & 0 & 0 \\ 0 & 0 & e^{-r_1} & 0 \\ 0 & 0 & 0 & e^{r_1} \end{pmatrix}. \quad (76)$$

The transformation matrix for the DHI can be obtained as $S_{\text{DHI}} = S_{\text{DOPA2}}S_{\text{BS}}S_{\theta}S_{\text{BS}}S_{\text{DOPA1}}$. Note that the S_{DOPA2} for the DHI is the same as that for the DSI. Therefore, the column vector of expected values of the quadratures for the output states and the input-output relation of the symmetric covariance matrix of the quadratures are

$$\bar{X}_{\text{DHI2}} = S_{\text{DHI}}\bar{X}_{\text{DHI1}}, \quad (77)$$

$$\Gamma_{\text{DHI2}} = S_{\text{DHI}}\Gamma_1 S_{\text{DHI}}^T \quad (78)$$

where $\bar{X}_{\text{DHI1}} = (0 \ |\alpha_{\text{DHI}}| \ 0 \ 0)^T$.

Then the QFI of the DHI can be obtained as

$$F_Q^{\text{DHI}} = 16\ell^2 \sinh^2(2r_1) + 4\ell^2 e^{4r_1} |\alpha_{\text{DSI}}|^2 = 16\ell^2 \sinh^2(2r_1) + 4\ell^2 e^{4r_1} I_{\text{PS}}^{\text{DHI}}. \quad (79)$$

According to Eq. (39), we can obtain the corresponding QCRB of the DHI.

These results are summarized in Fig. 8, showing the angular rotation sensitivity as a function of θ with the parameters $r_1 = r_2 = 1.15$, $I_{\text{PS}}^{\text{DHI}} = 10^3$, and $\ell = 2$ in the lossless scenario. The optimal sensitivity of the DHI has an enhancement of 5 dB compared with that of the MZI, which is better than that of the NHI. And the DHI has broader supersensitive angular rotation range than that of the DSI, which is approximately $\pi/8$. It is significant for improving the absolute sensitivity of the measurement while the supersensitive range still becomes broader for maintaining the measurement advantage.

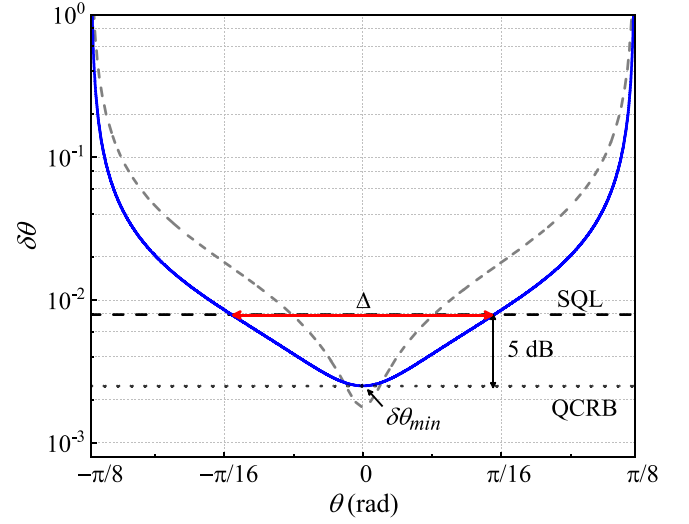


FIG. 8. Angular rotation sensitivity of a degenerate hybrid interferometer (Fig. 7) as a function of angular rotation θ , for the parameters $r_1 = r_2 = 1.15$, $I_{\text{PS}}^{\text{DHI}} = 10^3$, and $\ell = 2$ in the lossless scenario. The optimal angular rotation sensitivity $\delta\theta_{\text{min}}$ is obtained at $\theta = 0$. The supersensitive angular rotation range Δ is shown (red arrow). For comparison, the angular rotation sensitivity of the DSI (gray dashed line) from Fig. 4 is plotted as well.

III. ANALYSIS IN THE LOSSLESS SCENARIO

On the basis of the above, we calculate and compare the optimal sensitivities of different interferometers as a function of squeezing factor r_2 of the OPA2 in case of $r_1 = 1.15$, $I_{\text{PS}} = 10^3$, and $\ell = 2$ as shown in Fig. 9(a). It can be seen that the optimal sensitivities of the DSI and DHI remain constant with the squeezing factor r_2 increase. In other words, the optimal sensitivities of the DSI and DHI remain unaffected by the squeezing factor r_2 of the DOPA2 in the lossless scenario. However, for the NHI, as shown with the blue curve in Fig. 9(a), as the squeezing factor r_2 decreases, the sensitivity has a downward trend in a specific range. Especially, when the r_2 is less than 0.66, the sensitivity is even worse than the SQL. The phenomenon mainly comes from the imperfect detection process that only utilizes one of the entangled beams from the NOPA1 in the case of $r_2 = 0$. The beam has a higher noise variance than the vacuum state, resulting in worse sensitivity. As the squeezing factor r_2 increases, the phase-sensitive amplification with an opposite phase with the NOPA1 not only reduces the noise, but also amplifies the signal, hence improving the sensitivity of the NHI.

Figure 9(b) presents the sensitivity curves with the phase-sensing light intensity I_{PS} . It is shown that quantum-enhanced interferometers can achieve better measurement sensitivity than the MZI. When the phase-sensing light intensity I_{PS} increases from 10 to 1000, the sensitivity of the interferometers increases by one order of magnitude. Moreover, the sensitivity of the DSI is superior to that of other interferometers. However, for the DSI, the phase-sensing light intensity is restricted to a lower level, which becomes a primary bottleneck of applying to real systems. For the DHI, a coherent light is introduced into the MZI bright input port to increase I_{PS}

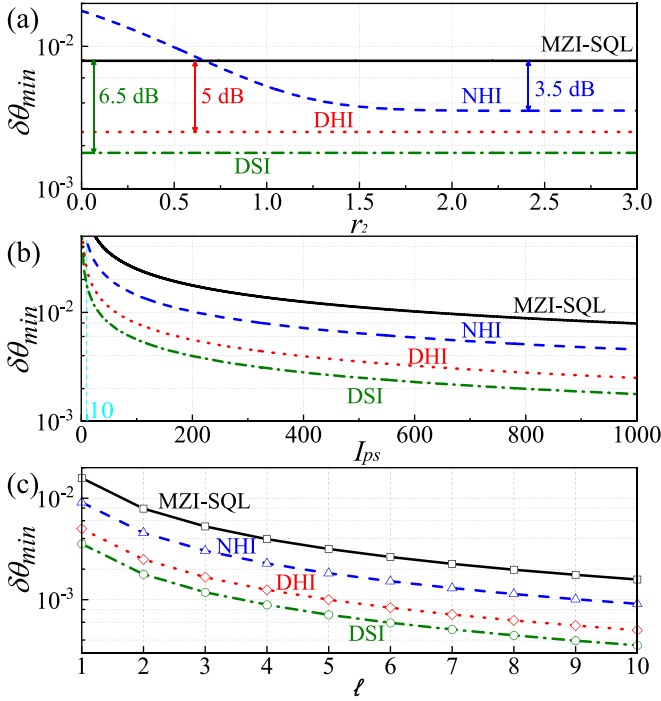


FIG. 9. (a) In the ideal case, the optimal sensitivities of four interferometers as a function of squeezing factor r_2 of the OPA2 ($r_1 = 1.15$, $I_{PS} = 10^3$, $\ell = 2$). (b) The optimal sensitivities of four interferometers as a function of phase-sensing light intensity I_{PS} in case $r_1 = r_2 = 1.15$, $\ell = 2$. (c) The optimal sensitivities of four interferometers as a function of OAM quanta number ℓ in case $r_1 = r_2 = 1.15$, $I_{PS} = 10^3$.

without introducing additional noise. That is, the DHI is easier to improve the measurement sensitivity than the DSI.

Figure 9(c) represents the optimal sensitivities of different interferometers versus the OAM quanta number ℓ . For these interferometers, when OAM quanta number ℓ increases, the sensitivities become better. However, the increasing ℓ reduces the quality of the generated beam and narrows supersensitive range, which can be obtained using Eqs. (26), (55), and (75).

IV. EFFECTS OF REALISTIC FACTORS

For practical interferometric measurements, except for internal losses, there always exist external losses due to imperfect elements or nonideal phase matching, etc., which makes the sensitivity worse. Supposing that the losses are linear, a VBS with transmissivity T_{ex} is placed in the output port of interferometers to simulate external losses, as shown in Fig. 10. Accordingly, the parameter $R_{ex} = 1 - T_{ex}$ can be used to represent external losses.

Under the situation when the system suffers from external losses, the expected value and the noise variance of \hat{X} are revised as follows:

$$\langle \hat{X}_l \rangle = \sqrt{T_{ex}} \langle \hat{X} \rangle, \quad (80)$$

$$\langle \delta^2 \hat{X}_l \rangle = T_{ex} \langle \delta^2 \hat{X} \rangle + R_{ex} \langle \delta^2 \hat{X}_\emptyset \rangle, \quad (81)$$

where R_{ex} is the reflectivity of the VBS; $\hat{\nu}$ is the annihilation operator for the vacuum state with noise variance $\langle \delta^2 \hat{X}_\emptyset \rangle = 1$.

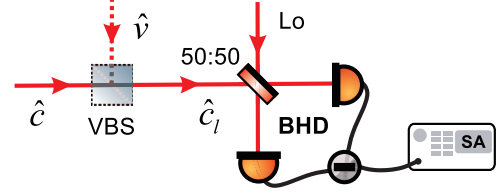


FIG. 10. Simplified model for external losses. A VBS is used to simulate photon losses. $\hat{\nu}$ is the operator for the vacuum state. VBS, virtual beam splitter; Lo, local oscillator; BHD, balanced homodyne detection; SA, spectrum analyzer.

According to the transformation relationships, we can obtain the optimal sensitivities of four interferometers in the case of $r_1 = r_2 = 1.15$, $I_{PS} = 10^3$, and $\ell = 2$ with T_{in} and T_{ex} , as manifested in Figs. 11(a) and 11(b), respectively. And keeping the internal losses in each arm the same, the influence of internal losses on sensitivity of angular rotation measurement is more severe than that of external losses. The sensitivities of angular rotation estimation gradually degrade with the decrease of the T_{ex} . Note that the gradient of the sensitivities decreases with the increase of the T_{ex} . We know from Fig. 11(b), that the DSI or DHI has better external-loss tolerance in an identical situation. Moreover, different from the NHI scheme, the DSI and DHI employ the DOPA to perform the quantum enhancement, which omit the application of the frequency converter [64].

Finally, we study the influence of the squeezing factor r_2 of the OPA2 on the sensitivities of angular rotation estimation for different quantum-enhanced interferometers in the lossy environment (external losses) (Fig. 12). We know from Eqs. (80) and (81) that the inevitable external losses during the measurement not only reduce the signal amplitude, but also introduce additional noise, resulting in measurement sensitivity degradation. The influence of the external losses on

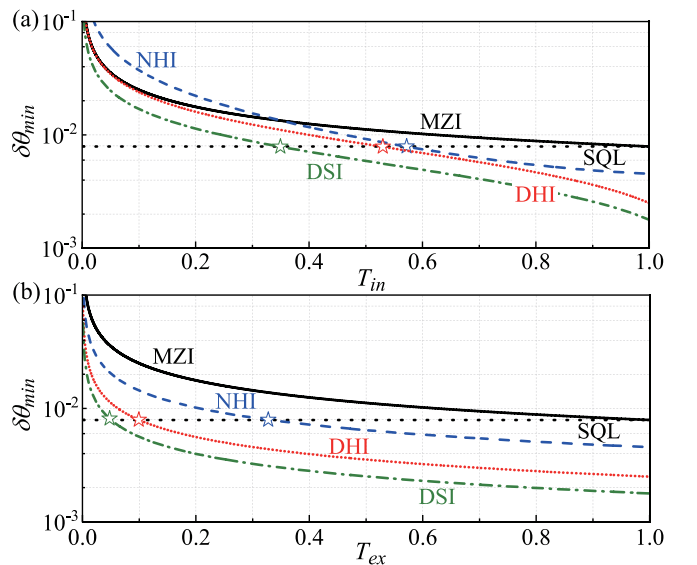


FIG. 11. Optimal angular rotation sensitivities $\delta\theta_{\min}$ in case $r_1 = r_2 = 1.15$, $I_{PS} = 10^3$, and $\ell = 2$ for different interferometers as a function of transmissivity (a) T_{in} and (b) T_{ex} , respectively. The stars indicate that the sensitivities of interferometers are equal to SQL.

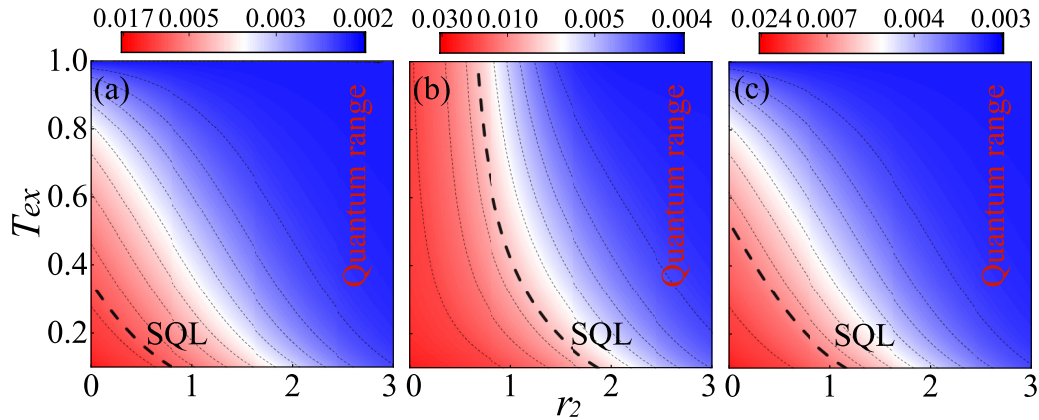


FIG. 12. Optimal sensitivities $\delta\theta_{\min}$ of the DSI (a), NHI (b), and DHI (c) with the squeezing factor r_2 of the OPA2 and transmissivity T_{ex} in case $r_1 = 1.15$, $I_{\text{ps}} = 10^3$, and $\ell = 2$.

the sensitivities of quantum-enhanced interferometers can be overcome by squeezing factor unbalancing for a given gain of the OPA1. As shown in Fig. 12, the sensitivity can be recovered by increasing the squeezing factor r_2 of the OPA2 until the sensitivity remains unchanged. And more external losses require more r_2 of the OPA2. That is to say, the estimation system becomes robust to external losses with the help of the OPA2. However, increasing r_2 cannot compensate the worsened sensitivity caused by the internal losses. The internal losses can be reduced by technological approaches, such as improving the mode-matching efficiency between two OPAs [25].

V. CONCLUSION

In summary, we have compared these performances of four different interferometers, including the external-loss-tolerant performance and the supersensitive range, for the application of angular rotation estimation. These results indicate that these different interferometers are perfectly applicable to angular rotation estimation. In virtue of quantum-enhanced schemes, we can obtain the sensitivity beyond SQL for

angular rotation estimation. Further, the sensitivity that is the same as in the case of no external losses can always be retrieved by taking full advantage of the second OPA as a phase-sensitive amplification. The DHI, combining the advantages of the DSI and MZI, can obtain the sensitivity enhancement beyond the SQL, external-loss-tolerant quantum noise reduction of the DSI, and broader supersensitive range of the MZI approach. These lay the foundation for experimental studies and provide the basis for sensitivity expression in a realistic scenario. We expect that this paper will extend the application field of optical interferometers and have potential applications in high-precision sensing and rotational Doppler shift measurement.

ACKNOWLEDGMENTS

This work was supported by the National Natural Science Foundation of China (Grants No. 62225504, No. 62027821, No. U22A6003, No. 62035015, No. 12174234, and No. 12304399) and Fundamental Research Program of Shanxi Province (Grants No. 202303021212003 and No. 202303021224006).

-
- [1] K. M. Backes, D. A. Palken, S. A. Kenany, B. M. Brubaker, S. B. Cahn, A. Droster *et al.*, A quantum enhanced search for dark matter axions, *Nature (London)* **590**, 238 (2021).
 - [2] J. Aasi, J. Abadie, B. P. Abbott, R. Abbott, T. D. Abbott, M. R. Abernathy *et al.*, Enhanced sensitivity of the LIGO gravitational wave detector by using squeezed states of light, *Nat. Photonics* **7**, 613 (2013).
 - [3] Y. Zhao, N. Aritomi, E. Capocasa, M. Leonardi, M. Eisenmann, Y. Guo *et al.*, Frequency-dependent squeezed vacuum source for broadband quantum noise reduction in advanced gravitational-wave detectors, *Phys. Rev. Lett.* **124**, 171101 (2020).
 - [4] L. McCuller, C. Whittle, D. Ganapathy, K. Komori, M. Tse, A. Fernandez-Galiana *et al.*, Frequency-dependent squeezing for advanced LIGO, *Phys. Rev. Lett.* **124**, 171102 (2020).
 - [5] A. Abramovici, W. E. Althouse, R. W. P. Drever, Y. Gürsle, S. Kawamura, F. J. Raab *et al.*, LIGO: The laser interferometer gravitational-wave observatory, *Science* **256**, 325 (1992).
 - [6] H. C. Yu, L. McCuller, M. Tse, N. Kijbunchoo, L. Barsotti, N. Mavalvala (the LIGO Scientific Collaboration), Quantum correlations between light and the kilogram-mass mirrors of LIGO, *Nature (London)* **583**, 43 (2020).
 - [7] B. P. Abbott, R. Abbott, T. D. Abbott, M. R. Abernathy, F. Acernese, K. Ackley *et al.*, Observation of gravitational waves from a binary black hole merger, *Phys. Rev. Lett.* **116**, 061102 (2016).
 - [8] T. Akutsu, M. Ando, K. Arai, K. Arai, Y. Arai, S. Araki *et al.*, An arm length stabilization system for KAGRA and future gravitational wave detectors, *Classical Quantum Gravity* **37**, 035004 (2020).

- [9] J. Heinze, A. Gill, A. Dmitriev, J. Smetana, T. Yan, V. Boyer, D. Martynov, and M. Evans, First results of the laser-interferometric detector for axions (LIDA), *Phys. Rev. Lett.* **132**, 191002 (2024).
- [10] V. Giovannetti, S. Lloyd, and L. Maccone, Quantum-enhanced measurements: Beating the standard quantum limit, *Science* **306**, 1330 (2004).
- [11] C. M. Caves, Quantum-mechanical noise in an interferometer, *Phys. Rev. D* **23**, 1693 (1981).
- [12] S. P. Shi, L. Tian, Y. J. Wang, Y. H. Zheng, C. D. Xie, and K. C. Peng, Demonstration of channel multiplexing quantum communication exploiting entangled sideband modes, *Phys. Rev. Lett.* **125**, 070502 (2020).
- [13] X. C. Sun, Y. J. Wang, Y. H. Tian, Q. W. Wang, L. Tian, Y. H. Zheng, and K. C. Peng, Deterministic and universal quantum squeezing gate with a teleportation-like protocol, *Laser Photonics Rev.* **16**, 2100329 (2022).
- [14] A. N. Boto, P. Kok, D. S. Abrams, S. L. Braunstein, C. P. Williams, and J. P. Dowling, Quantum interferometric optical lithography: Exploiting entanglement to beat the diffraction limit, *Phys. Rev. Lett.* **85**, 2733 (2000).
- [15] J. P. Dowling, Quantum optical metrology: The lowdown on high-N00N states, *Contemp. Phys.* **49**, 125 (2008).
- [16] F. Hudelist, J. Kong, C. J. Liu, J. T. Jing, Z. Y. Ou, and W. P. Zhang, Quantum metrology with parametric amplifier-based photon correlation interferometers, *Nat. Commun.* **5**, 3049 (2014).
- [17] X. J. Zuo, Z. H. Yan, Y. N. Feng, J. X. Ma, X. J. Jia, C. D. Xie, and K. C. Peng, Quantum interferometer combining squeezing and parametric amplification, *Phys. Rev. Lett.* **124**, 173602 (2020).
- [18] S. Balybin, D. Salykina, and F. Ya. Khalili, Improving the sensitivity of Kerr quantum nondemolition measurement via squeezed light, *Phys. Rev. A* **108**, 053708 (2023).
- [19] X. T. Chen, R. Zhang, W. J. Lu, Y. L. Zuo, Y. F. Jiao, and L. M. Kuang, Asymmetry-enhanced phase sensing via asymmetric entangled coherent states, *Phys. Rev. A* **109**, 042609 (2024).
- [20] Z. Y. Ou, Enhancement of the phase-measurement sensitivity beyond the standard quantum limit by a nonlinear interferometer, *Phys. Rev. A* **85**, 023815 (2012).
- [21] T. Gefen, R. Tarafder, R. X. Adhikari, and Y. B. Chen, Quantum precision limits of displacement noise-free interferometers, *Phys. Rev. Lett.* **132**, 020801 (2024).
- [22] B. E. Anderson, P. Gupta, B. L. Schmittberger, T. Horrom, C. Hermann-Avigliano, K. M. Jones, and P. D. Lett, Phase sensing beyond the standard quantum limit with a variation on the SU(1, 1) interferometer, *Optica* **4**, 752 (2017).
- [23] P. M. Anisimov, G. M. Raterman, A. Chiruvelli, W. N. Plick, S. D. Huver, H. Lee, and J. P. Dowling, Quantum metrology with two-mode squeezed vacuum: Parity detection beats the heisenberg limit, *Phys. Rev. Lett.* **104**, 103602 (2010).
- [24] R. Demkowicz-Dobrzanski, U. Dorner, B. J. Smith, J. S. Lundeen, W. Wasilewski, K. Banaszek, and I. A. Walmsley, Quantum phase estimation with lossy interferometers, *Phys. Rev. A* **80**, 013825 (2009).
- [25] L. Tian, W. X. Yao, Y. M. Wu, Q. W. Wang, H. Shen, Y. H. Zheng, and K. C. Peng, Loss-tolerant and quantum-enhanced interferometer by reversed squeezing processes, *Opt. Lett.* **48**, 3909 (2023).
- [26] M. Manceau, G. Leuchs, F. Khalili, and M. Chekhova, Detection loss tolerant supersensitive phase measurement with an SU(1, 1) interferometer, *Phys. Rev. Lett.* **119**, 223604 (2017).
- [27] W. Du, J. Kong, G. Z. Bao, P. Y. Yang, J. Jia, S. Ming, C. H. Yuan, J. F. Chen, Z. Y. Ou, M. W. Mitchell, and W. P. Zhang, SU(2)-in-SU(1, 1) nested interferometer for high sensitivity, loss-tolerant quantum metrology, *Phys. Rev. Lett.* **128**, 033601 (2022).
- [28] M. Korobko, J. Südbeck, S. Steinlechner, and R. Schnabel, Fundamental sensitivity limit of lossy cavity-enhanced interferometers with external and internal squeezing, *Phys. Rev. A* **108**, 063705 (2023).
- [29] D. Gatto, P. Facchi, and V. Tamma, Heisenberg-limited estimation robust to photon losses in a Mach-Zehnder network with squeezed light, *Phys. Rev. A* **105**, 012607 (2022).
- [30] X. N. Feng, D. He, and L. F. Wei, Robust phase metrology with hybrid quantum interferometers against particle losses, *Phys. Rev. A* **107**, 062411 (2023).
- [31] A. B. Matsko and S. P. Vyatchanin, Standard quantum limit of sensitivity of an optical gyroscope, *Phys. Rev. A* **98**, 063821 (2018).
- [32] A. G. Krause, M. Winger, T. D. Blasius, Q. Lin, and O. Painter, A high-resolution microchip optomechanical accelerometer, *Nat. Photonics* **6**, 768 (2012).
- [33] S. Barnett and R. Zambrini, Resolution in rotation measurements, *J. Mod. Opt.* **53**, 613 (2006).
- [34] O. S. Magaña-Loaiza, M. Mirhosseini, B. Rodenburg, and R. W. Boyd, Amplification of angular rotations using weak measurements, *Phys. Rev. Lett.* **112**, 200401 (2014).
- [35] Z. J. Zhang, T. Y. Qiao, K. Ma, L. Z. Cen, J. D. Zhang, F. Wang, and Y. Zhao, Ultra-sensitive and super-resolving angular rotation measurement based on photon orbital angular momentum using parity measurement, *Opt. Lett.* **41**, 3856 (2016).
- [36] S. X. Xiao, L. D. Zhang, D. Wei, F. Liu, Y. Zhang, and M. Xiao, Orbital angular momentum-enhanced measurement of rotation vibration using a Sagnac interferometer, *Opt. Express* **26**, 1997 (2018).
- [37] J. X. Guo, S. Ming, Y. Wu, L. Q. Chen, and W. P. Zhang, Super-sensitive rotation measurement with an orbital angular momentum atom-light hybrid interferometer, *Opt. Express* **29**, 208 (2021).
- [38] M. Hiekkamäki, F. Bouchard, and R. Fickler, Photonic angular superresolution using twisted N00N states, *Phys. Rev. Lett.* **127**, 263601 (2021).
- [39] M. Pancaldi, F. Guzzi, C. S. Bevis, M. Manfredda, J. Barolak, S. Bonetti *et al.*, High-resolution ptychographic imaging at a seeded free-electron laser source using OAM beams, *Optica* **11**, 403 (2024).
- [40] N. Uribe-Patarroyo, A. Fraine, D. S. Simon, O. Minaeva, and A. V. Sergienko, Object identification using correlated orbital angular momentum states, *Phys. Rev. Lett.* **110**, 043601 (2013).
- [41] X. Y. Fang, H. C. Yang, W. Z. Yao, T. X. Wang, Y. Zhang, M. Gu, and M. Xiao, High-dimensional orbital angular momentum multiplexing nonlinear holography, *Adv. Photonics* **3**, 015001 (2021).
- [42] M. Bourennane, A. Karlsson, and G. Björk, Quantum key distribution using multilevel encoding, *Phys. Rev. A* **64**, 012306 (2001).

- [43] A. Vaziri, G. Weihs, and A. Zeilinger, Experimental two-photon, three-dimensional entanglement for quantum communication, *Phys. Rev. Lett.* **89**, 240401 (2002).
- [44] J. T. Barreiro, T. C. Wei, and P. G. Kwiat, Beating the channel capacity limit for linear photonic superdense coding, *Nat. Phys.* **4**, 282 (2008).
- [45] L. Chen and W. She, Teleportation of a controllable orbital angular momentum generator, *Phys. Rev. A* **80**, 063831 (2009).
- [46] M. Mafu, A. Dudley, S. Goyal, D. Giovannini, M. McLaren, M. J. Padgett, T. Konrad, F. Petruccione, N. Lütkenhaus, and A. Forbes, Higher-dimensional orbital-angular-momentum-based quantum key distribution with mutually unbiased bases, *Phys. Rev. A* **88**, 032305 (2013).
- [47] G. Vallone, V. D'Ambrosio, A. Sponselli, S. Slussarenko, L. Marrucci, F. Sciarrino, and P. Villoresi, Free space quantum key distribution by rotation-invariant twisted photons, *Phys. Rev. Lett.* **113**, 060503 (2014).
- [48] A. E. Willner, H. Huang, Y. Yan, Y. Ren, N. Ahmed, G. Xie, C. Bao, L. Li, Y. Cao, Z. Zhao, J. Wang, M. P. J. Lavery, M. Tur, S. Ramachandran, A. F. Molisch, N. Ashrafi, and S. Ashrafi, Optical communications using orbital angular momentum beams, *Adv. Opt. Photonics* **7**, 66 (2015).
- [49] A. Nicolas, L. Veissier, L. Giner, E. Giacobino, D. Maxein, and J. Laurat, A quantum memory for orbital angular momentum photonic qubits, *Nat. Photonics* **8**, 234 (2014).
- [50] G. Molina-Terriza, J. P. Torres, and L. Torner, Twisted photons, *Nat. Phys.* **3**, 305 (2007).
- [51] M. Erhard, R. Fickler, M. Krenn, and A. Zeilinger, Twisted photons: New quantum perspectives in high dimensions, *Light: Sci. Appl.* **7**, 17146 (2018).
- [52] M. Padgett and R. Bowman, Tweezers with a twist, *Nat. Photonics* **5**, 343 (2011).
- [53] P. J. L. Martin, F. C. Speirits, S. M. Barnett, and M. J. Padgett, Detection of a spinning object using light's orbital angular momentum, *Science* **341**, 632 (2013).
- [54] N. Cvijetic, G. Milione, E. Ip, and T. Wang, Detecting lateral motion using light's orbital angular momentum, *Sci. Rep.* **5**, 15422 (2015).
- [55] J. Wang, W. Zhang, Q. Qi, S. Zheng, and L. Chen, Gradual edge enhancement in spiral phase contrast imaging with fractional vortex filters, *Sci. Rep.* **5**, 15826 (2015).
- [56] D. G. Grier, A revolution in optical manipulation, *Nature (London)* **424**, 810 (2003).
- [57] N. Bozinovic, Y. Yue, Y. Ren, M. Tur, P. Kristensen, H. Huang, A. E. Willner, and S. Ramachandran, Terabit-scale orbital angular momentum mode division multiplexing in fibers, *Science* **340**, 1545 (2013).
- [58] Y. J. Chen, J. W. Gao, J. X. Han, Z. H. Yuan, R. Q. Li, Y. Y. Jiang, and J. Song, Orbital-angular-momentum-enhanced phase estimation using non-Gaussian states with photon loss, *Phys. Rev. A* **108**, 022613 (2023).
- [59] V. D'Ambrosio, N. Spagnolo, L. Del Re, S. Slussarenko, Y. Li, L. C. Kwek, L. Marrucci, S. P. Walborn, L. Aolita, and F. Sciarrino, Photonic polarization gears for ultra-sensitive angular measurements, *Nat. Commun.* **4**, 2432 (2013).
- [60] J. Courtial, K. Dholakia, D. A. Robertson, L. Allen, and M. J. Padgett, Measurement of the rotational frequency shift imparted to a rotating light beam possessing orbital angular momentum, *Phys. Rev. Lett.* **80**, 3217 (1998).
- [61] R. Fickler, R. Lapkiewicz, W. N. Plick, M. Krenn, C. Schaeff, S. Ramelow, and A. Zeilinger, Quantum entanglement of high angular momenta, *Science* **338**, 640 (2012).
- [62] J. Liu, W. X. Liu, S. T. Li, D. Wei, H. Gao, and F. L. Li, Enhancement of the angular rotation measurement sensitivity based on SU(2) and SU(1, 1) interferometers, *Photonics Res.* **5**, 617 (2017).
- [63] J. Liu, S. T. Li, D. Wei, H. Gao, and F. L. Li, Super-resolution and ultra-sensitivity of angular rotation measurement based on SU(1, 1) interferometers using homodyne detection, *J. Opt.* **20**, 025201 (2018).
- [64] J. Liu, C. Y. Wang, J. W. Wang, Y. Chen, R. F. Liu, D. Wei, H. Gao, and F. L. Li, Super-sensitive measurement of angular rotation displacement based on the hybrid interferometers, *Opt. Express* **27**, 31376 (2019).
- [65] G. A. Turnbull, D. A. Robertson, G. M. Smith, L. Allen, and M. J. Padgett, The generation of free-space Laguerre-Gaussian modes at millimetre-wave frequencies by use of a spiral phase plate, *Opt. Commun.* **127**, 183 (1996).
- [66] A. M. Yao and M. J. Padgett, Orbital angular momentum: Origins, behavior and applications, *Adv. Opt. Photonics* **3**, 161 (2011).
- [67] A. K. Jha, G. S. Agarwal, and R. W. Boyd, Supersensitive measurement of angular displacements using entangled photons, *Phys. Rev. A* **83**, 053829 (2011).
- [68] M. J. Padgett and J. P. Lesso, Dove prisms and polarized light, *J. Mod. Opt.* **46**, 175 (1999).
- [69] I. Moreno, G. Paez, and M. Strojnik, Polarization transforming properties of Dove prisms, *Opt. Commun.* **220**, 257 (2003).
- [70] M. Manceau, F. Khalili, and M. Chekhova, Improving the phase super-sensitivity of squeezing-assisted interferometers by squeeze factor unbalancing, *New J. Phys.* **19**, 013014 (2017).
- [71] S. P. Shi, Y. J. Wang, L. Tian, W. Li, Y. M. Wu, Q. W. Wang, Y. H. Zheng, and K. C. Peng, Continuous variable quantum teleportation network, *Laser Photonics Rev.* **17**, 2200508 (2023).
- [72] X. C. Sun, Y. J. Wang, L. Tian, S. P. Shi, Y. H. Zheng, and K. C. Peng, Dependence of the squeezing and anti-squeezing factors of bright squeezed light on the seed beam power and pump beam noise, *Opt. Lett.* **44**, 1789 (2019).
- [73] D. Li, B. T. Gard, Y. Gao, C. H. Yuan, W. P. Zhang, H. Lee, and J. P. Dowling, Phase sensitivity at the Heisenberg limit in an SU(1, 1) interferometer via parity detection, *Phys. Rev. A* **94**, 063840 (2016).
- [74] B. E. Anderson, B. L. Schmittberger, P. Gupta, K. M. Jones, and P. D. Lett, Optimal phase measurement with bright- and vacuum-seeded SU(1, 1) interferometers, *Phys. Rev. A* **95**, 063843 (2017).